# TIGHT COUPLING OF HELICOPTER AIRFRAME INCLUDING A DETAILED GEARBOX

Oskar Wengrzyn, Institut für Aerodynamik und Gasdynamik, Universität Stuttgart, Stuttgart, Germany
Lennart Frie, Institut für Technische und Numerische Mechanik, Universität Stuttgart, Stuttgart, Germany
Manuel Keßler, Institut für Aerodynamik und Gasdynamik, Universität Stuttgart, Stuttgart, Germany
Ewald Krämer, Institut für Aerodynamik und Gasdynamik, Universität Stuttgart, Stuttgart, Germany
Peter Eberhard, Institut für Technische und Numerische Mechanik, Universität Stuttgart, Stuttgart, Germany

**Abstract**

Until recently vibrations in helicopters could only be measured or anticipated with high levels of uncertainty. This changed when tools focused on coupling started to emerge offering to combine both state-of-the-art fluid and structural dynamics solutions. This enables to predict the fluid-structure-interactions in the design phase which is an invaluable addition to the engineer's toolbox. The presented work shows the results of a tightly coupled CSD-CFD simulation of a helicopter in forward flight. The trimming process is shown and followed by an analysis of energy distribution across the modes. The aerodynamic origins of the excitations are investigated based on the pressure distribution and vortex visualization. The influence of a detailed gearbox to the CSD model is estimated by comparing the results from two different CSD models.

## 1. INTRODUCTION

Over the years, vibration prediction in helicopter design has proven to be a difficult task. The nature of helicopters requires the accurate prediction of both, structural dynamics and aerodynamics to capture the character of the vibrations. Both, high fidelity structural and aerodynamic domains require significant computational resources, and the multidisciplinary nature of the problem requires collaboration between experts in both fields. Many researchers have tackled the vibration problem, but only recently have vibrations been accurately predicted in Ref. 1 after decades of continuous progress in aeromechanics and high-performance computing.

Various mechanical systems have been developed to combat extensive vibrations. These solutions enabled researchers to significantly reduce the accelerations perceived by the crew. From the 1960s to 1980s they decreased from *0.4g* to as low as *0.1g* as shown in Ref. 2. Unfortunately, the frequency range of helicopter vibrations overlaps with the range of increased human sensitivity according to the ISO 2631 norm. As a result, the passenger and crew comfort is still compromised, although significant progress has been made in reducing cabin accelerations. Future designs objective is to further reduce the perceived vibrations and achieve "jet-smooth" ride characteristics.

The inability to predict the vibration levels during the design phase is one of the reasons that testing with prototypes is a necessity as shown in Ref. 3 and 4. This process also adds a risk factor to the flight test campaigns, which often show that additional vibration reduction devices are required to reduce the amplitudes of the loads transmitted to the airframe.

The testing process is expensive and time consuming, but for a long time it was the only way to gain insight into the world of helicopter vibrations. This began to change in the 1990s as the increased availability of computational power enabled tools such as CAMRAD II. CAMRAD II uses simplified aerodynamic and structural dynamics models to predict fluid-structure interaction. Therefore, the representation of physics in CAMRAD II is less accurate than modern computational fluid dynamics (CFD) and computational structural dynamics (CSD) approaches. However, CAMRAD II's major advantage is its low computational cost and the speed of the analysis. Both are very valuable in the design phase where tens or hundreds of designs need to be evaluated. General airframe vibration characteristics could be predicted and the addition of a coupled simulation to the design toolbox proved successful.

An accurate CSD model is still required as an input. The model should include an accurate representation of the airframe, gearbox, and a load path between them. The presented requirements can lead to unpractical size and complexity of the model. As a result, various techniques have been developed to reduce the degrees of freedom, and consequently the complexity of the model. Those techniques allow accurate prediction of the dominant phenomena at relatively low computational cost.

In parallel with the CSD, the aerodynamics community has continued to further develop CFD. The unique flow characteristics of helicopters, such as the wide range of Mach numbers, separation, reverse flow, and vortex interactions, pose significant difficulties for the CFD solver. Codes specializing in helicopter aerodynamics began to emerge - such as FLOWer described in Ref. 5. Continuous development of FLOWer also introduced deformable geometries and an interface between various tools commonly used in the industry, allowing for trimming of the flight state. The CFD solver also takes advantage of parallelization which leads to efficient use of high-performance computing.

All the mentioned advancements lead to the state-of-the-art coupled simulation where for the first time tailshake was predicted, see Ref. 1. The simulation couples high-fidelity CFD and state-of-the-art CSD to obtain a time-resolved solution. The results were validated against flight test data with good agreement between the two data sets. This method allows to test various designs at reasonable computational effort which proves invaluable in understanding the helicopter's vibrations, in order to develop appropriate countermeasures.

The present work builds on the aforementioned state of the art coupled simulation. For a tailshake prediction, the low frequency range is of most importance. The main excitation source is the wake impinging tail boom and tail planes, so the vibrations coming from the main rotor and the elasticity of the gearbox are of low importance. This requires an accurate airframe model, but the gearbox can be simplified. On the other hand, the gearbox is expected to be an important component in cabin vibration prediction as found in Ref. 6. In the presented case, a detailed gearbox has been added to the CSD model allowing not only the tailshake to be predicted, but also the cabin vibrations and rotor hub displacement. The influence of the detailed gearbox will be presented.

## 2. FLIGHT STATE AND SIMULATION TOOLS

The helicopter selected for this study is an experimental configuration. It uses experimental BK117 airframe combined with a new rotor design described in Ref. 7. The setup was designed as a proof of concept for the GRC1 rotor which consists of five bearingless blades.

The research is focused on a fast forward flight denoted as TOP35. The advance ratio $\mu$ is equal to 0.31. The fast forward flight includes the effects of the asymmetric inflow combined with separation on the retreating blade and Mach number effects on the advancing side. This leads to a high nonuniformity of the flow field, resulting in an increase in vibration levels as shown in Ref. 2.

### 2.1. CFD solver

The CFD code used in this study was developed at the German Aerospace Center (DLR) and is called FLOWer. It is a structured Reynolds-averaged Navier-Stokes (RANS) finite volume code. The SST k-ω turbulence model is used to close the RANS equations. The equations are integrated over time using an implicit dual time stepping algorithm according to Jameson, (see Ref. 8). Throughout the years, the code has been continuously improved at the Institute for Aerodynamics and Gas dynamics (IAG) at the University of Stuttgart. Recent improvements that are key to coupled simulations include:

- 5th order spatial WENO schemes,
- grid deformation calculated using radial basis functions (RBF), and
- implementation of engines inlet and outlet boundary conditions with temperature distribution and swirl.

The increased order of spatial resolution helps to resolve finer turbulence structures and reduces their dissipation. This leads to more uniform distribution of the energy across the frequency range as the finer structures carry energy in the higher frequency range, see Ref. 9. The grid deformation based on RBF functions ensures that the surface remains smooth and free of any mesh errors and, as stated in Ref. 10, including the engine wake and inflow is crucial in tail-shake predictions.

The helicopter's control angles and attitudes are controlled by an external trimming tool, here CAMRAD II. FLOWer has been modified to include not only the rigid body motions extracted from CAMRAD II, but also the main rotor blade deformations. This ensures that a proper flight state is maintained in the computational domain. Additionally, the structured mesh is split into smaller blocks, which leads to good scaling with the number of compute cores.

### 2.2. CSD solver

The deformations of the structure are calculated using a 2nd order Newmark integration method described in Ref. 11. The solver assumes a linear variation of acceleration between time steps and is considered unconditionally stable for linear problems. It is embedded in the CFD code, which means that the memory is shared between the solvers. This significantly reduces the complexity of data exchange and takes advantage of code scaling. The solution is computed in modal space, allowing flexibility in the CSD modelling. Any order reduction scheme can be used to decrease the size of the problem. The inputs to the solver include mass, stiffness, and mode shape matrices. These can be obtained from any FEM software that offers export of real eigenvalue analysis results. For NASTRAN an automated pre-processing framework is available which extracts the required data from an output file. The final input required is the CSD mesh file which is used by an automated pre-processor to map the CSD and CFD meshes. The mapping is then sent to FLOWer, which applies the calculated CFD loads to the nearest CSD node at each time step.

### 2.3. Structural coupling

In general, two types of coupling can be distinguished: partitioned and monolithic coupling. The monolithic scheme combines both fluid and structure equations into a single solver. The order of the method is dependent on the chosen time integrator. Monolithic codes can be considered as the ideal coupling schemes, but their validation and implementation prove to be challenging or not possible at all. The equations describing simultaneously the structure and fluid dynamics quickly become complicated and require simplifications, which therefore usually restrict the equations to a narrow field of applications. The software also lacks modularity and can be difficult to integrate into a toolbox. Reference 12 gives an overview of the advantages and disadvantages of monolithic codes.

The more popular type of coupling uses partitioned schemes. These consist of separate solvers specializing in their own subset of the problem. This approach is easier to implement as often out-of-the-box software can be coupled together. This limits the development effort required to prepare an interface between the two tools. The flexibility of the solver choice is valuable since popular and validated solvers can be coupled, which makes their implementation easier and potentially useful for more cases.

Partitioned schemes usually follow staggered algorithms during the simulation run. A typical staggered algorithm is shown in Figure 1. For a CSD/CFD coupled simulation the steps are as follows:

1) calculate the current CFD time step,

2) transfer the resulting loads to the CSD tool,

3) solve the CSD equations of motion,

4) transfer the deformation to the CFD and deform the mesh.

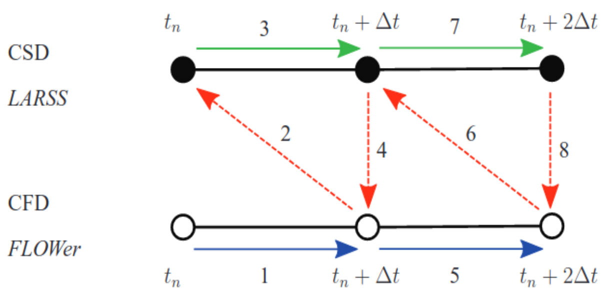


Figure 1 Gauss-Seidel algorithm. Figure adapted from Ref. 1

This staggered algorithm is called Gauss-Seidel algorithm or commonly “ping pong”. The downsides of this algorithm include a low order of time accuracy and poor numerical stability. However, Ref. 12 shows examples of second-order time-accurate coupling using the partitioned method.

The mentioned “ping-pong” algorithm is used here to couple CSD and CFD solvers. In this coupling scheme, the data exchange occurs at every time step, and it is common to refer to such workflows as strong coupling amongst the rotorcraft community. One cycle represents one physical time step, leading to the deformation being delayed by one time step. In Ref. 1, the author estimates the resulting phase error to be less than 8 degrees for the higher frequency modes and less than 1 degree for the lower frequency with time step of 1 degree of MR azimuth.

### 2.4. Trimming

To accurately model the loads applied to the structure, a trimmed flight state must first be calculated. A partitioned loose coupling interface known as HeliCATS was used for this task. The tool uses the comprehensive analysis code CAMRAD II to trim the flight state based on the forces calculated by the CFD solver FLOWer. The tool was supplied by Airbus Helicopters and is described in Ref. 13.

The HeliCATS' workflow is shown in Figure 2. An iteration begins with a CAMRAD II run, which calculates the control angles, attitudes, and the deformations of the main rotor blades. The CFD input files are then modified to include the correct control angles, attitudes, and blade's kinematics. The CFD job is calculated, and the resulting forces and moments are processed such that they can be used as input in the next CAMRAD II run. CAMRAD II's calculations are initially based on rotor and fuselage polars provided by the user. At every HeliCATS iteration *n*, the polar based loads are corrected by the forces calculated by FLOWer according to:

$$F_T^n = F_{2D}^n + (F_{CFD}^{n-1} - F_{2D}^{n-1}), \quad (1)$$

where $F_T^n$ denotes loads used in the comprehensive code for the trim task, $F_{2D}^n$ are the loads calculated using polars and $F_{CFD}^n$ are the loads from CFD calculation. The rotor loads are provided as a function of the blade azimuth, whereas the fuselage loads are averaged. This approach allows for trimming of only steady-state flight cases, i.e. hover, forward flight or steady turns. More information can be found in Ref. 14.

## 3. DISCRETE MODELS

### 3.1. CFD model

The discrete model used in CFD calculations consists of around 90 million cells. The mesh was designed with the Chimera overset grid technique in mind, which allows overlapping grids to exchange data.

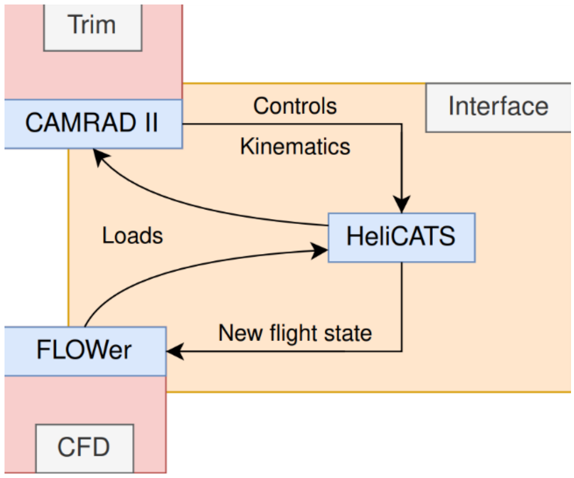


Figure 2 HeliCATS workflow

As a result, complex geometries can be split into individual components that are easier to mesh. The presented setup consists of 44 individually meshed parts.

The grid can be categorized into two sub-groups: body and off-body grids. The body grid has a maximum spatial resolution of 0.1 times the main rotor blade chord length *c*. The mesh is extruded in the normal direction with growth ratios between 1.1 for rotor blades and 1.4 for parts of the airframe. The extrusion spans up to 2*c* with the initial cell size ensuring y+ values below one. The off-body mesh is automatically generated and of a Cartesian type. It uses hanging nodes to adapt the spatial resolution around user-specified areas. The off-body grid also has a resolution of 0.1*c* around the whole body and rotor blades.

The setup is shown in Figure 3. The airframe is colored orange while the skids, main rotor and horizontal stabilizers are shown in dark blue. The CFD uses WENO and models the engines outlet and inlet boundary conditions. The engine's inlets and outlets together with the Fenestron stators are colored light blue. The Fenestron also includes individual blades with accurate blade spacing between them. The main rotor hub is not included in the domain as it would increase the mesh size significantly. Consequently, blades' roots are also omitted. As shown in Ref. 1, the wake of the main rotor hub contributes to the tail-shake phenomenon, so neglecting the main rotor hub will affect the presented results by changing the wake structure. However, this simplification is considered acceptable in order to reduce the computational effort required.

However, the main rotor hub node is included in the CSD domain and the CFD's main rotor rotates around it. This means that any deformation of the main rotor hub calculated by the CSD solver is included in the CFD. Additionally, it is assumed that the Fenestron duct, blades, and stators are rigid and exactly follow the hub node in the CSD domain. This assumption is necessary to prevent the mesh of the Fenestron blades from penetrating the surface of the duct, which would cause stability problems in the CFD. The deformations of the main rotor blades are calculated by an external tool during the trimming process. The resulting kinematics of the blades are then frozen.

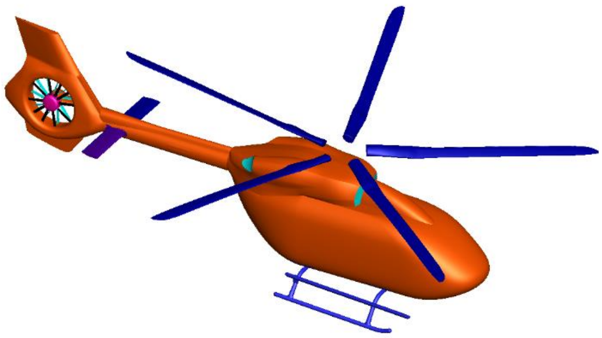

Figure 3 CFD setup

### 3.2. CSD model

In modern aerospace engineering, the design and analysis of helicopter fuselages is increasingly reliant on advanced computational methods. The finite element method (FEM) provides a powerful tool for simulating the structural behaviour of helicopter fuselages under various operational conditions. The industrial finite element model that is used here is shown in Figure 4.

At this stage, some important points need to be highlighted. The main rotor and fenestron are not included in the finite element (FE) model and are instead represented by surrogate masses. This also applies to the side doors and windows. It can be seen that the resolution of the tail boom mesh is much finer compared to that of the cabin. These three facts influence the forces acting on the nodes of the FE model. Since some parts are not fully resolved, the force from the surrounding CFD cells is summed up and applied to a few substitute nodes that are the closest to CFD cells. Consequently, large forces are observed at the hub nodes of the main rotor and the Fenestron, as well as at the surrogate nodes in the centre of the doors, windows and their frames.

While the coupling process accounts for these model simplifications, in order to be conservative, it has to be mentioned that they still limit the accuracy of the simulation. Despite that, the FE model remains highly detailed, with hundreds of thousands of degrees of freedom. This results in a high numerical cost of transient simulation and motivates the use of Model Order Reduction (MOR), which aims to represent the full-order system with a low-rank approximation while preserving its key properties.

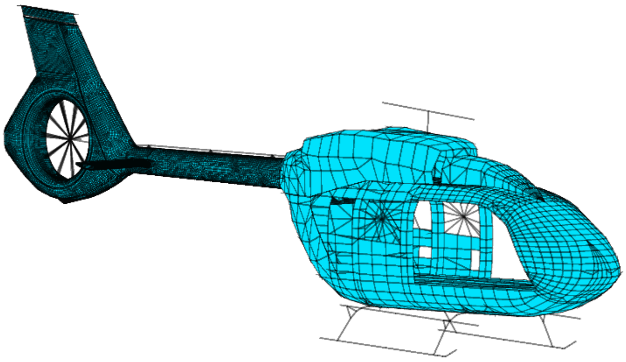

Figure 4 Industrial finite element model used for the coupled simulation

The finite element method yields a second-order differential equation of the form

(2) $$M\ddot{q}(t) + Kq(t) = f.$$

Here, the matrices $M \in \mathbb{R}^{N\,x\,N}$ and $K \in \mathbb{R}^{N\,x\,N}$ are the mass matrix and the stiffness matrix, respectively.

The vector $q \in \mathbb{R}^{N}$ describes the displacements of the finite element nodes. The time derivatives are notated with $\dot{q}(t) \coloneqq \frac{dq(t)}{dt}$ and $\ddot{q}(t) \coloneqq \frac{d^2q(t)}{dt^2}$.

To reduce the order of the model, projection-based MOR is used. In projection-based MOR, the goal is to approximate the full-order system in a subspace $\mathcal{V}$ of much lower dimension. This subspace is spanned by the so-called projection matrix $V$ with

(3) $$\mathcal{V} = span\,\{V\}.$$

The projection matrix is built with the eigenmodes $\phi_i$ of the model. The first *n* eigenmodes are used, which yields

(4) $$V = [\phi_1, \phi_2, \ldots, \phi_n] \in \mathbb{R}^{N\,x\,n} \text{ with } n \ll N.$$

All other modes are truncated. For noticeable cabin vibrations, the low frequency range up to about 40Hz is especially relevant. The first 40 eigenfrequencies of the finite element model are in the range up to 45Hz so that they can describe a major part of the deformation behaviour. The reduced model is obtained by a Galerkin-projection

$$\overbrace{V^T M V}^{M_r}\,\ddot{q}_t(t) + \overbrace{V^T K\, V}^{K_r}\,q_t(t) = Vf(t), \tag{5}$$

with the reduced quantities $M_r \in \mathbb{R}^{n\,x\,n}$, $K_r \in \mathbb{R}^{n\,x\,n}$, and $q_r \in \mathbb{R}^n$.

The eigenmodes diagonalize the system. With the normalized projection matrix

$$\bar{V} = (V^T M_t V)^{-1} V, \tag{6}$$

the reduced mass matrix becomes the identity, and the reduced stiffness matrix consists of the squared eigenfrequencies with

$$K_t = diag(\omega_i^2),\ i = 1,\ 2, \ldots, n, \tag{7}$$

where $\omega_i$ are radial eigenfrequencies. Damping is considered with a modal damping model. Therefore, the modal damping matrix

$$D_t = diag(2\varsigma\omega_i),\ i = 1, 2, \ldots, n \tag{8}$$

with the modal damping ratio $\varsigma$ is added to Equation 4. This yields the reduced representation of the damped system

$$M_t\ddot{q}(t) + D_t\dot{q}(t) + K_t q(t) = \bar{V}f(t). \tag{9}$$

The structural damping is set to 2% in all the simulations presented in this work. It is worth noting that other MOR approaches that are not based on eigenmodes are also possible, further details can be found in Refs. 15 and 16.

## 4. TRIMMED STATE

The trimmed state is calculated using HeliCATS. Initially, ten revolutions are calculated with artificially chosen control angles and rigid rotor blades to obtain a representative flow-field. Afterwards, HeliCATS is started and the CFD uses the previously obtained flow-field as a restart point. The trim includes six degrees of freedom (DoF): three main rotor control angles, Fenestron blades' pitch, and fuselage's roll and pitch attitudes. The seventh degree of freedom, which is in this case the yaw angle, is fixed to a constant value. To ensure a proper CFD solution, the data is exchanged every two main rotor revolutions. The first revolution is calculated to make sure the flow field adapted to the new flight state, and the loads from the second revolution were used for the trimming process.

The convergence of the trimmed solution is determined based on the residual accelerations calculated according to the equations:

$$r_p^T = \frac{\sum F_p}{m},\ r_p^A = \frac{\sum M_p}{I_p}, \tag{10}$$

where *p* represents a given axis, $F_p$ and $M_p$ are the force and moment along axis *p*; *m* is the mass of the helicopter and $I_q$ is the inertia over axis *p*. The values of the residuals must be below a certain threshold for the flight state to be considered trimmed. The threshold values were taken from Ref. 17 and therefore must obey

$$\left|r_p^T\right| < 0.1\frac{m}{s^2} \quad and \quad \left|r_p^A\right| < 1\frac{deg}{s^2}. \tag{11}$$

Initially, all the control angles and attitudes oscillate around some value with the highest deviations at the Fenestron's pitch angle. This results from the weak coupling scheme stability conditions being broken. The stability conditions as determined in Ref. 13 require that the CFD's force gradient over trim variable must be:

- of the same sign as the gradient calculated by CAMRAD II and
- less than twice of the gradient calculated by CAMRAD II.

CAMRAD II uses the Newton-Raphson algorithm to calculate the trimmed state. The method requires a calculation of the Jacobian matrix based on the polars and CAMRAD II's internal aerodynamics model. The polars are usually based on CFD simulations or wind tunnel tests, but the internal aerodynamics of CAMRAD II uses significant simplifications.

Fenestron rotors are particularly problematic as they are only considered on a time averaged basis. They can be considered exactly the same way as the main rotor blade, however it is not practical as the complexity of the HeliCATS setup would increase significantly, especially for Fenestron rotors with uneven blade spacing. This led to the development of a workaround where the CFD loads of the Fenestron's duct and hub are considered to be a part of the CAMRAD II's fuselage. The fuselage polar is then shifted to match the CFD loads.

CAMRAD II also does not include blade necks in its computation, but they are included in the CFD domain. The main rotor blades are treated differently compared to the Fenestron as they are elastic. Here, an interface is used that allows the CFD loads to be applied to the individual panels. Those panels represent parts of the blade in the comprehensive tool. CFD's rotor blade mesh is much finer than the panel representation used in CAMRAD II. This requires mapping between each CFD node to a corresponding panel. The loads from the blade necks are transferred to the innermost panel. Alternatively, the loads from the blade necks can also be applied to the fuselage.

To investigate the solution oscillations described previously, a stability analysis was conducted. The analysis included calculating a Jacobian matrix in the CFD domain and comparing it to the CAMRAD II's estimation. The CFD Jacobian matrix calculation included twelve simulations. Each simulation had one control angle or attitude changed by $\Delta x_i = 0.5°$. The new blade deformations were calculated for each of the simulations using CAMRAD II and the gain results from

$$gain = \frac{f(x_i+\Delta x_i)-f(\Delta x_i)}{\Delta x_i}, \quad (12)$$

where $x_i$ is the given control angle/attitude. The comparison of both Jacobian matrices allowed the identification of the problems with the setup. The Fenestron parameters in CAMRAD II were adjusted to match the gain of CFD. An artificial force was applied to the airframe that was equal to the Fenestron's hub and duct loads, but in the opposite direction. The loads from the blade necks were also attributed to the fuselage, which further improved stability. Figures 5 and 6 show the values of the residual accelerations as function of the HeliCATS' iterations. Both figures also show the threshold values marked as red, horizontal lines.

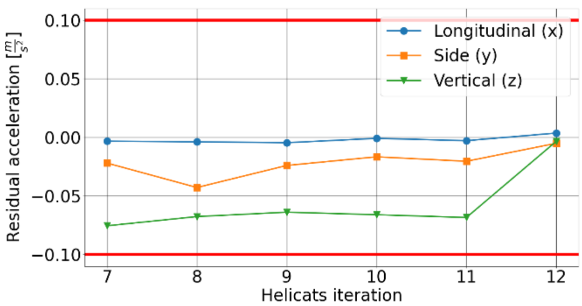


Figure 5 Example of residual translational accelerations

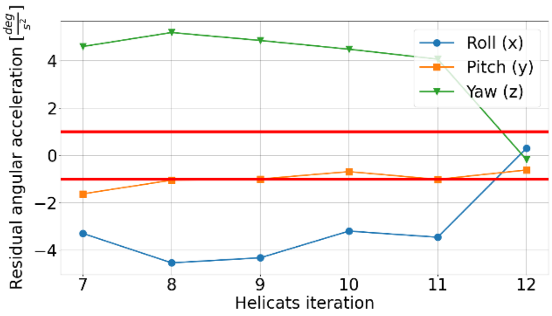


Figure 6 Example of residual angular accelerations

The trimmed case includes a rigid airframe. It is possible to trim the flight state with an elastic airframe enabled but it would require a CSD model with proper representation of the static deformations. Static deformations are not a focus in the scope of this work. The effort is mostly put into modeling the dynamic part of the deformations. The deformations also present some stochastic behavior (see Ref. 8), which would require longer CFD run times. When using the controls from the rigid case with an elastic airframe, the deformations change the state of the helicopter, resulting in an increase in the residual accelerations. The residuals are compared in Table 1. The residual accelerations of the elastic case are outside of the threshold values, but it is anticipated that their influence on the overall vibration characteristics can be omitted. To give a better understanding of the physical meaning, the largest residual of angular acceleration (yaw) corresponds to an additional 35N of thrust at the Fenestron.

Table 1 Residual accelerations of rigid and elastic cases

| Residual acceleration along axis in [$\frac{m}{s^2}$] | | | |
|---|---|---|---|
| | Vertical | Longitudinal | Traverse |
| Rigid | 0.004 | -0.005 | -0.003 |
| Elastic | 0.028 | 0.020 | -0.068 |
| **Residual acceleration around axis in [$\frac{deg}{s^2}$]** | | | |
| | Yaw | Roll | Pitch |
| Rigid | 0.313 | -0.630 | 0.210 |
| Elastic | -3.447 | -1.001 | 4.060 |

## 5. Results

The presented results were calculated using the previously described strong coupling toolchain. The elastic simulation was started from a trimmed rigid state calculated using HeliCATS. The airframe is elastic, the main rotor hub motions are included in the CFD. The rigid body motions are not included in the CFD domain.

Two CSD models will be compared that differ in the representation of the gearbox. The simplified gearbox is represented by a rigid housing with lumped mass and the detailed gearbox refers to a detailed finite element model (DFEM). The results presented in sections 5.1 and 5.2 are calculated using the detailed gearbox representation.

### 5.1. Airframe deformation and error estimation

The absolute mean deformation of the airframe is shown in Figure 7. The mean value is calculated over two main rotor revolutions. The largest deformation occurs at the top of the vertical stabilizer, followed by the Fenestron and the right horizontal stabilizer. The structure at the front of the helicopter is deflected by a similar amount as the Fenestron.

The root-mean-square (RMS) values are shown in Figure 8. Here, the vertical stabilizer oscillates most. The tail boom together with the front of the cabin is mostly affected by the mean deformation as the RMS values are close to zero. The horizontal stabilizers deviate almost the same amount compared to each other, even though they present different mean deformations. The skids, cabin roof, and area around the doors present similar RMS values.


Figure 7 Mean deformations of the airframe

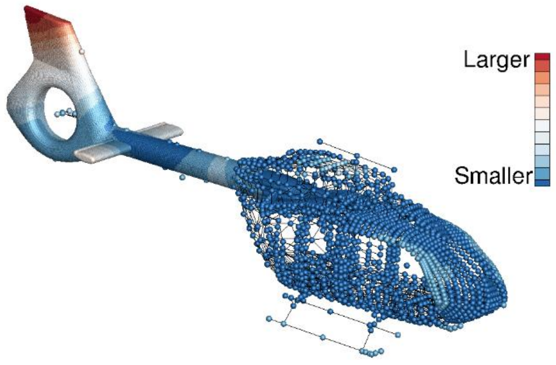


Figure 8 Root-mean-square of the deformation

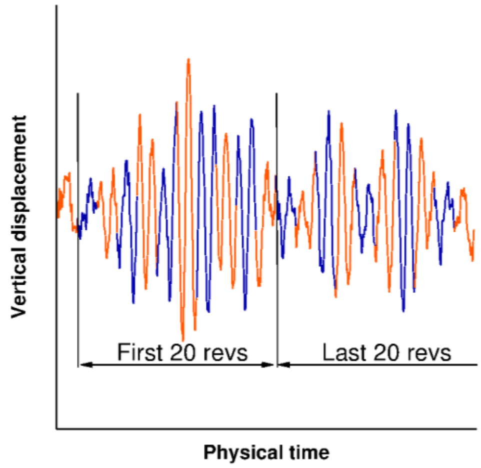


Figure 9 Vertical deformation of the main rotor hub as function of time

Figure 9 shows the vertical deformation of the main rotor hub as a function of time. Each color in the graph represents two main rotor revolutions calculated in CFD. The graph shows a total of 42 revolutions with the first two being disregarded as they were used as an adjustment period for the CFD solution. This adjustment period was necessary as the simulation was restarted from a converged rigid case.

To estimate the CFD error, the FFT of the first 20 revolutions was compared to the FFT of the last 20. A period of 20 revolutions corresponds to over 3.1 seconds of physical time, which captures the complete period of the lowest frequency eigenmode multiple times. Such a long run also ensures that the FFT resolution is high enough to compare the non-harmonic contributions. The relative error is then calculated using

$$(13)\quad error = \frac{FFT(node_i)_{last\ 20\ revs} - FFT(node_i)_{first\ 20\ revs}}{FFT(node_i)_{first\ 20\ revs}}.$$

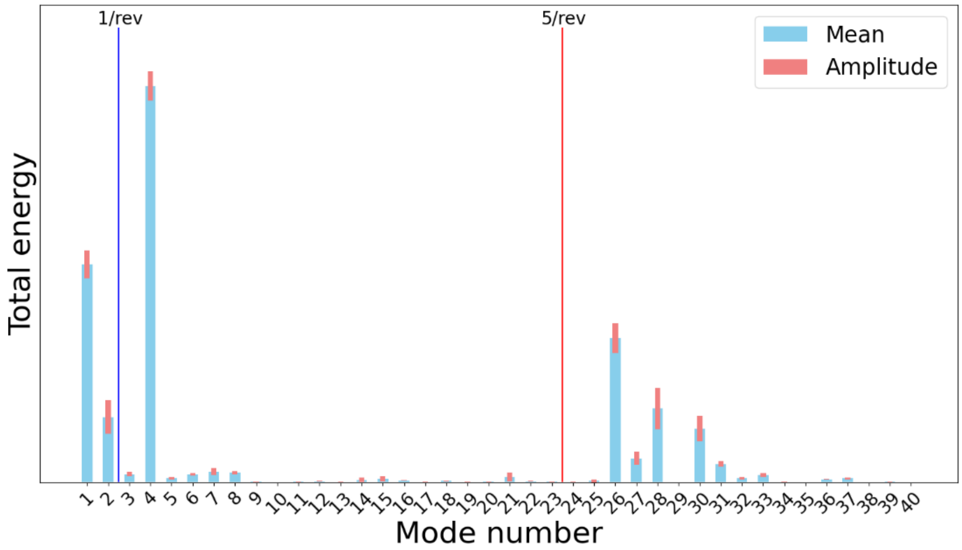


Figure 10 Energy distribution per mode

For the peaks at harmonic frequencies the error was less than 5%, whereas for the non-harmonic frequencies, it was below 30%.

From Figure 9 it can be clearly seen that the deformation varies significantly over time and no clear period can be identified. The low frequency influence that can be seen corresponds to the first eigenfrequency of the airframe.

The distribution of the energy over the modes is shown in Figure 10. The mean value of the energy function is represented by the blue bars while its amplitude is represented by the red bars. Both values were averaged over a period of 20 revolutions. The modes are sorted by their eigenfrequency in ascending order. For additional information the 1/rev and 5/rev frequencies are plotted using blue are red vertical lines. It can be seen that the 1/rev frequency lies between eigenfrequencies of modes 2 and 3 and 5/rev is located between modes 23 and 24. The 4$^{th}$ mode has the highest energy content which is over double that of the next largest contributor to the deformation: mode number 1. Modes 1 and 4 dominate with another significant contribution coming from higher frequency modes 26, 28 and 30. The 1$^{st}$ and 4$^{th}$ modes are responsible for vertical bending, whereas mode number 2 is horizontal bending. The higher frequency modes in the range between 26 and 30 are mostly responsible for horizontal stabilizers bending and twisting as well as the deformation of skids, roof and the area around the doors.

The energy content was calculated with

$$E = \frac{1}{2\,|\xi|^2}\left(m\dot{u}^2 + ku^2\right), \tag{14}$$

where $E$ stands for total energy, $|\xi|$ is the length of mode shape vector, $m$ is the modal mass, $k$ is the modal stiffness and $u$ is the deformation. The term $ku^2$ is the strain energy responsible for the mean deformation of the structure. The term $m\dot{u}^2$ is the energy of the dynamic part of the deformation shown as amplitudes.

However, looking at the energy graph does not give a complete overview of the deformation. Shapes of modes 1 and 4 are both responsible for vertical bending, however when both are multiplied by the same artificial amplitude, they deform the structure in the opposite direction. This results in a mean deformation smaller than what would be expected by just simply looking at the energy graph. Similarly, the large amplitudes of some modes would suggest that they are responsible for a large part of the cabin vibration. However the corresponding mode shapes have their nodes located around the cabin area, which results in small contributions to cabin vibrations. It is also important to note that all modes carry some energy and contribute to total deformation.

### 5.2. Pressure distribution

The aeromechanical nature of the underlying problem requires an analysis of both the pressure distribution and the mechanical forces. Since the problem is indeed “aeromechanical” and not “mechanicalaero” it is clear that the pressure distribution is more important and therefore, its analysis will follow.

Figures 12, 13, 14 and 15 show the FFT of pressure at the CFD surface over a period of 10 revolutions. Four frequency regions of interest can be distinguished: below 1/rev, between 1 and 4.8/rev, between 4.8/rev, and 5.2/rev and finally above 5.2/rev. Each interval is left-open. The mentioned figures show a sum of amplitudes at frequencies within each group plotted using the same scale for an easier comparison.

Figure 12 presents the frequency range above 5.2/rev, which shows large pressure amplitudes at the front of the cabin and at the roof. These areas correspond very well to the anti-nodes of the mode shapes 26, 28 and 30 resulting in an excitation. A flow field analysis is in place to understand the distribution of the pressure amplitudes.

Looking at the $\lambda_2$ visualization shown in Figure 11, separation can be seen at the advancing blade’s neck which is most likely responsible for the pressure variations around the roof of the cabin. Similarly, the wake from the engine and fuselage interacts with the vertical stabilizer which causes a separation to form on its leading edge. This separation can be seen as region of high-pressure variations in Figure 12. To explain the variations at the front of the cabin, an FFT of the volumetric solution is plotted in Figure 16. A clear vortex pattern can be seen, with its wake interacting with the cabin’s surface leading to pressure variation.

As the considered helicopter uses a five bladed rotor, the frequency range between 4.8 and 5.2/rev shown in Figure 13 is expected to have the largest amplitudes. However, looking at Figure 12 it can be seen that the amplitudes at frequencies above 5.2/rev are higher. It seems that the previously described separation and vortex interaction cause significant amplitudes of pressure fluctuations. The distribution of the pressure fluctuations is similar to the distribution at frequencies above 5.2/rev. The modes 21 to 24 have their eigenfrequencies within the 4.8 to 5.2/rev range, but they are mostly responsible for bending of the horizontal stabilizers and twisting of the skids. The pressure fluctuations do not suggest any excitation of those modes and they indeed carry little energy, see Figure 10.

A look at Figure 14 might lead to a conclusion that mode number 4 is excited due to the pressure variations at the front of the cabin as this is also the location of the mode’s anti-node, but a closer look around its eigenfrequency in Figure 17 reveals almost no variation of pressure at that frequency. This suggests that mode number 4 is excited due to the spatial distribution of the loads. Given its small energy amplitude, it can be concluded that the pressure variations

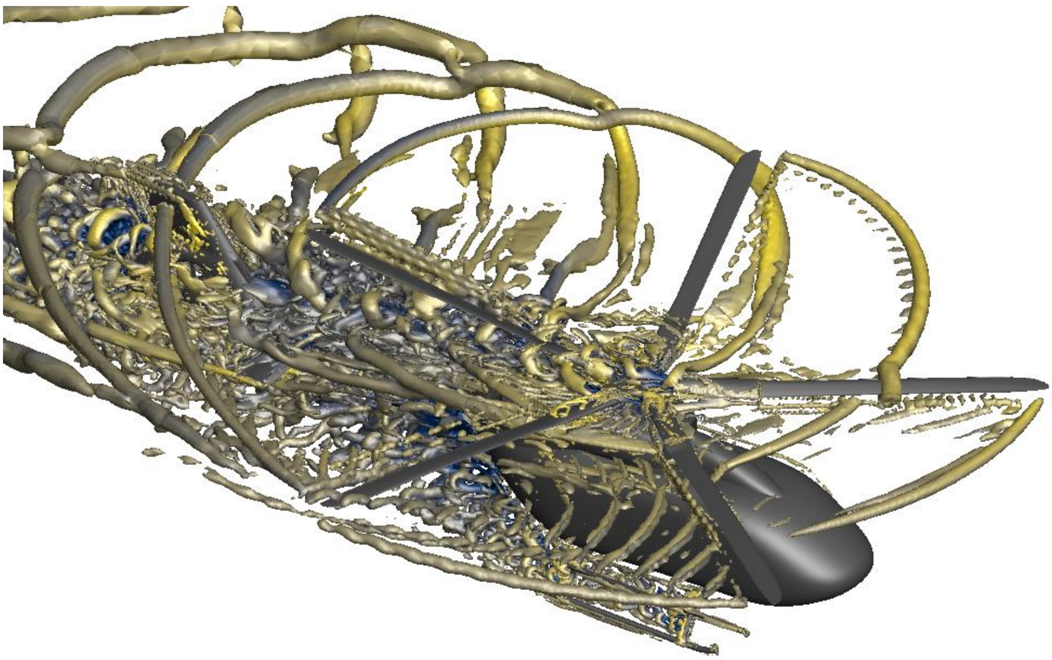

Figure 11 $\lambda_2$ vortex visualization colored by local velocity present at the Fenestron do not supply enough energy to cause large oscillations of this mode.

For the presented case, this method of analyzing the pressure variations and comparing them to mode shapes only works for the frequencies above 5.2/rev. Looking at Figure 15 which shows the pressure amplitudes at frequencies below 1/rev, no clear excitation source can be seen. The largest amplitudes are located around the Fenestron, but the values are relatively low. However, the low frequency modes can be easily excited as their modal stiffness and damping are low. The spatial frequency or wavelength of the low frequency modes is also lower which makes them more susceptible to excitations, as the forces need not to be highly concentrated at the anti-nodes. It is possible that the spatial distribution of the loads is responsible for supplying the modes with high energy and that the pressure variations at the Fenestron are enough to cause the oscillations of the deformations.

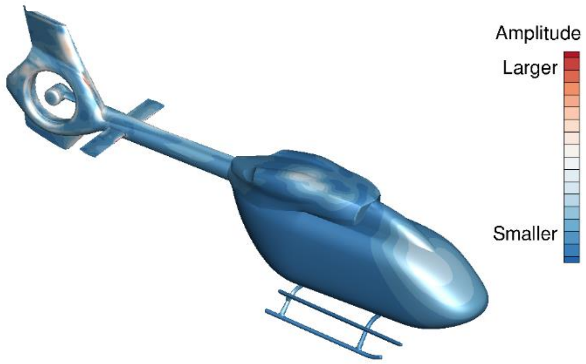


Figure 12 Pressure variations at frequencies above 5.2/rev

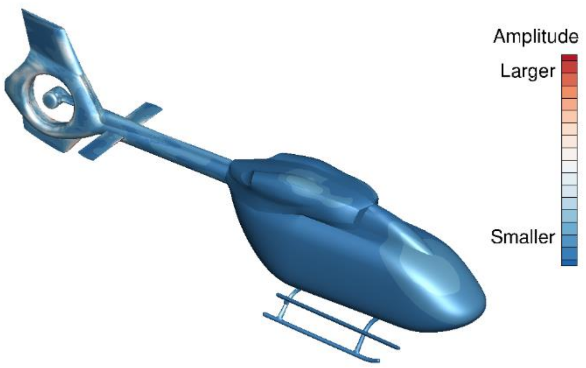


Figure 13 Pressure variations at frequencies between 4.8 and 5.2/rev

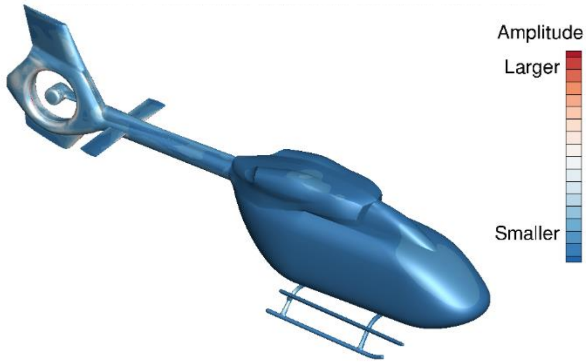


Figure 14 Pressure variations at frequencies between 1 and 4.8/rev

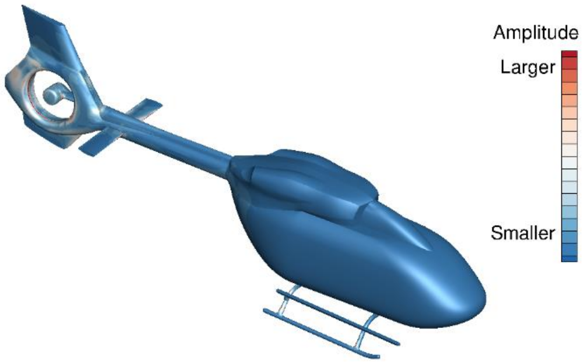


Figure 15 Pressure variations at frequencies below 1/rev

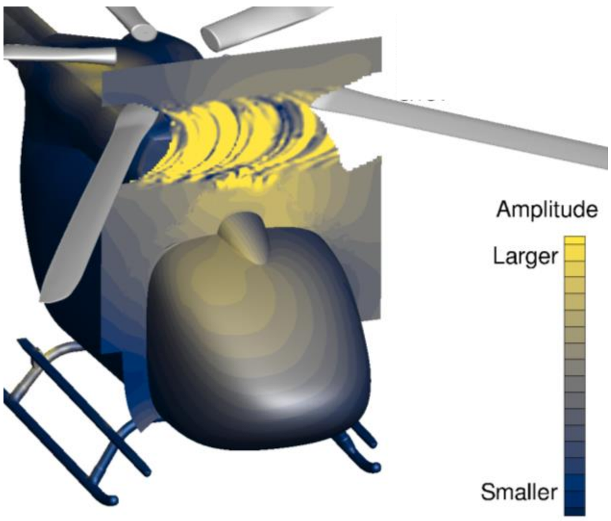


Figure 16 Pressure variations at frequencies above and including 5/rev around the cabin

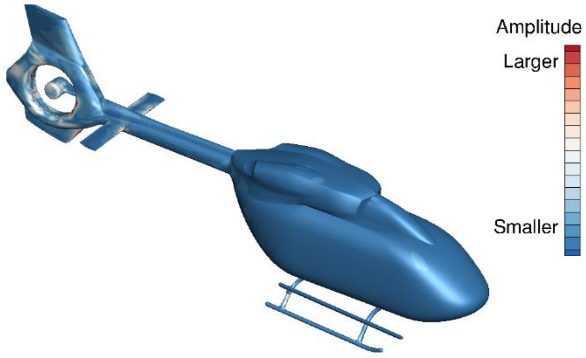


Figure 17 Pressure variations at eigenfrequency of mode no. 4

### 5.3. Accelerations

From the perspective of the passengers' and crew's comfort, cabin accelerations are crucial. The Fourier transform of the accelerations at the cabin floor is plotted in Figure 18. In this case a period of twenty main rotor revolutions is considered. Clearly the largest amplitude is present at 5/rev with low non-harmonic contributions at around 4/rev. The non-harmonic components are almost an order of magnitude smaller than the value at the 5/rev. The vertical acceleration dominates, followed by longitudinal and lateral.

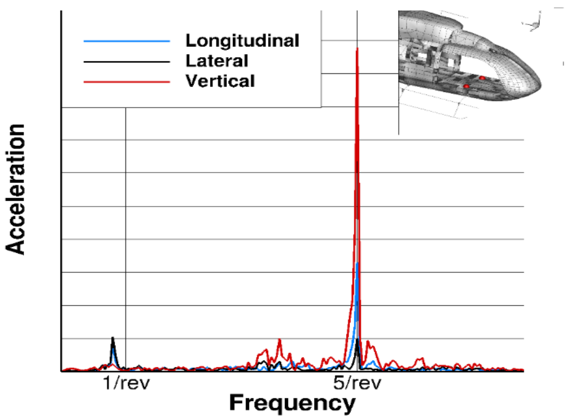


Figure 18 Cabin floor accelerations

The presented results are based on a new and improved CSD model that includes a detailed gearbox. To evaluate the impact of gearbox on the accelerations, results using both CSD models are plotted in Figure 19. The two models are compared based on vertical accelerations since they dominate the cabin floor. As can be seen, the addition of a detailed gearbox model leads to a higher value of acceleration at the cabin floor with the non-harmonic components being comparable between the two models.

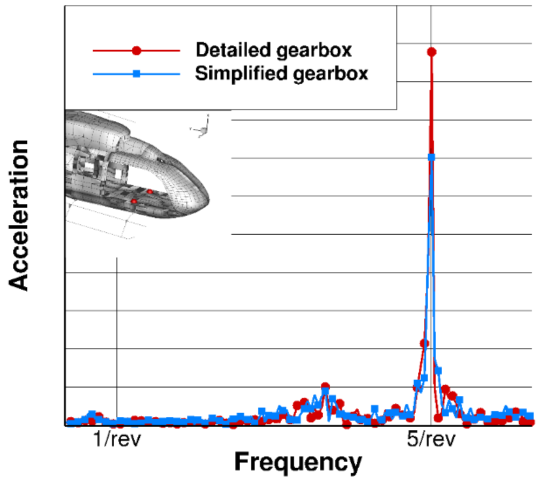


Figure 19 Vertical acceleration at cabin floor: comparison of the two CSD models

It is also interesting to look at the accelerations at the main rotor hub, which are plotted in Figure 20. As expected, the largest peak is at 5/rev frequency, but also a significant contribution around 4/rev frequency is present in the spectrum. This 4/rev peak corresponds to the eigenfrequency of mode number 11 and the mode is mostly responsible for skids deformation and longitudinal motions of the main rotor hub. Other eigenfrequencies are also marked on the plot to explain the cluster of peaks at frequencies just below 4/rev as well as the small peak below 1/rev. Even though only couple of modes carry significant values of energy all of them contribute to deformation of the structure which can clearly be seen here.

The largest accelerations calculated using the CSD models with different gearbox model are compared in Figure 21. Similarly to the cabin floor, the model with detailed gearbox predicts higher amplitudes at 5/rev frequency. Both models have similar solutions below 4/rev, but the model with detailed gearbox predicts a large non-harmonic component at around 4/rev. This is completely skipped by the model with simplified gearbox. On the other hand, the model with simplified gearbox predicts non-harmonic accelerations around 6/rev which are not present in the prediction with detailed gearbox. This tendency remains for other airframe points and is probably due to the differences in response functions of both CSD models.

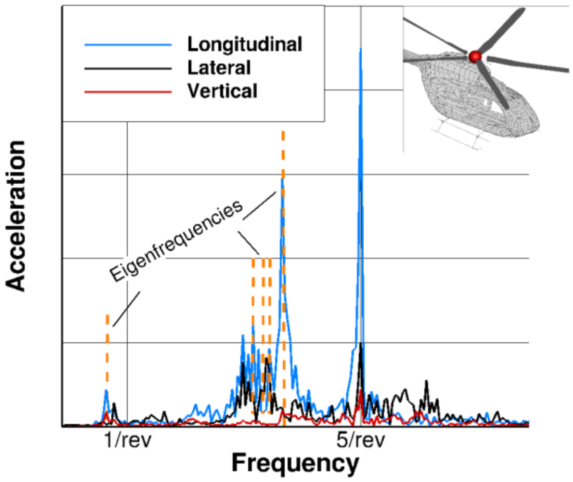


Figure 20 Main rotor hub accelerations

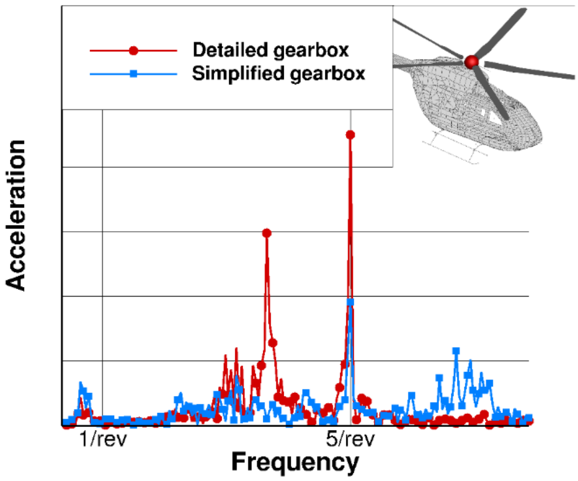


Figure 21 Lateral acceleration at the main rotor hub: comparison of the two CSD models

## 6. CONCLUSIONS

The conclusions based on the data presented in this paper are as follows:

- The Jacobian matrix calculated using a CFD solver can be helpful in improving the coupling scheme.
- The deformation of the airframe changes the flight state of the helicopter, but trimming with elastic airframe enabled would require long run times as more revolutions must be calculated to properly represent the deformed state.
- The largest deformation of the structure occurs at the vertical stabilizer.
- The fundamental modes like horizontal and vertical bending carry the most energy.
- The low frequency modes are most likely excited due to the spatial distribution of the loads as the low-frequency fluctuations have low amplitudes.
- Higher frequency modes are also present in the deformation as they are excited by pressure fluctuations.
- The addition of a detailed gearbox to the structural model significantly changes the predicted accelerations both in the cabin and at the hub.
- Some modes, even though they do not carry significant energy, can still be seen in the accelerations at the main rotor hub.

The next steps would be to validate the results with flight test data. That way it could be determined if the addition of a detailed gearbox helped with the accuracy of the vibration prediction. Nonetheless, the presented tool chain proves that it can work with state-of-the-art CSD models and help in the development of future generations of helicopters.

## ACKNOWLEDGMENTS

The authors acknowledge the support provided by the German Federal Ministry for Economic Affairs and Climate Action in the framework of the EVOLVE research project (FKZ 20A1902C). We also thank Airbus Helicopters and especially Oliver Dieterich for the valuable discussions. Further acknowledgment is made to the High-Performance Computing Center (HLRS) in Stuttgart who provided us with support and service to perform the computations on their high-performance computing system Hawk.

Supported by:

Federal Ministry
for Economic Affairs
and Climate Action

on the basis of a decision
by the German Bundestag

## REFERENCES

[1] U. Schäferlein, M. Keßler, and E. Krämer, “Aeroelastic Simulation of the Tail Shake Phenomenon,” in *43rd European Rotorcraft Forum*, Milan, Italy, Sep. 2017.

[2] G. Reichert, “Helicopter vibration control: a survey,” in *6th European Rotorcraft and Powered Lift Air-craft Forum Proceedings*, Bristol, Sep. 1980.

[3] H. Huber and T. Masue, “Flight Characteristics Design and Development of the MBB/KHI BB 117 Helicopter,” in *7th European Rotorcraft and Powered Lift Aircraft Forum Proceedings*, Garmisch-Partenkirchen, Germany, Sep. 1981.

[4] K. Kampa, B. Enenkl, G. Polz, and G. Roth, “Aeromechanic Aspects in the Design of the EC135,” in *23rd European Rotorcraft Forum Proceedings*, Dresden, Germany, Sep. 1997.

[5] N. Kroll, B. Eisfeld, and H. Bleeke, “The Navier Stokes code FLOWer,” *Notes on Numerical Fluid Mechanics*, vol. 71, pp. 58–71, 1999.

[6] R. Sopher, R. E. Studwell, S. Cassarino, and S. B. R. Kottapalli, “Coupled rotor/airframe vibration analysis,” in *NASA Technical Reports*, 1982.

[7] A. Kus, S. Schneider, M. Hollands, R. Rammer, O. Dieterich, and M. Priems, “GRC1: An Advanced Five-Bladed Bearingless Main Rotor Dynamics and Acoustics from Draft to Flight Test,” in *AHS International 74th Annual Forum & Technology Display*, Phoenix, Arizona, 2018.

[8] A. Jameson, “Time dependent calculations using multigrid, with applications to unsteady flows past air-foils and wings,” in *AIAA 10th Computational Fluid Dynamics Con-ference*, Honolulu, Hawaii, 1991.

[9] U. Schäferlein, *Numerical Investigation of Aeroacustic and Aeroelastic Phenomena on a Helicopter Using Higher-Order Methods*. Verlag Dr. Hut, 2018.

[10] P. G. De Waard and M. Trouvé, “Tail shake vibration: Objective comparison of aerodynamic configurations in a subjective en-vironment,” in *American Helicopter Society 55th Annual Forum*, Montreal, Canada, 1999.

[11] N. M Newmark, “A Method of Computation for Structural Dynamics,” *Journal of the Engineering Mechanics Division*, vol. 85, no. 3, pp. 67–94, 1959.

[12] C. Farhat, K. G. van der Zee, and P. Geuzaine, “Provably second-order time-accurate loosely-coupled solution algorithms for transient non-linear computational aeroelasticity,” *Comput Methods Appl Mech Eng*, vol. 195, no. 17–18, pp. 1973–2001, 2006.

[13] M. Embacher, M. Keßler, M. Dietz, and E. Krämer, “Coupled CFD-Simulation of a Helicopter in Free-Flight Trim,” in *66th American Helicopter Society Annual Forum*, Phoenix, Arizona, May 2010.

[14] A. Altmikus, S. Wagner, P. Beaumier, and G. Servera, “A Comparison: Weak versus Strong Modular Coupling for Trimmed Aeroelastic Rotor Simulations,” in *American Helicopter Society 58th Annual Forum*, Montreal, Canada, 2002.

[15] Manuel Vierneisel, Lennart Frie, and Peter Eberhard, “Model Order Reduction – Also with Many Inputs and Outputs?,” *EasyChair Preprint no. 13282*, 2024.

[16] L. Frie and P. Eberhard, “On shift selection for Krylov subspace based model order reduction,” *Multibody Syst Dyn*, vol. 58, no. 3, pp. 231–251, 2023, doi: 10.1007/s11044-022-09872-7.

[17] U. Kowarsch, C. Öehrle, M. Keßler, and E. Krämer, “Aeroacoustic Simulation of a Complete (H145) Helicopter In Descent Flight,” in *41st European Rotorcraft Forum*, Munich, Germany, Sep. 2015.

## CLASSIFICATION & COPYRIGHT